The Journal of Geometric Analysis (2023) 33:309
https://doi.org/10.1007/s12220-023-01342-6

Animal Shapes, Modal Analysis, and Visualization of Motion (II): Dynamics and Fourier Decomposition

Goong Chen[1,2,3] · **Chunqiu Wei**[4] · **Alexey Sergeev**[1] · **Jing Yang**[5] · **Jingtong Kaya Huang**[1] · **Matthew M. Scully**[1] · **Ming-Chieh Chen**[6] · **Steven G. Krantz**[7] · **Pengfei Yao**[8,9] · **Tiexin Guo**[10] · **Junmin Wang**[5]

Received: 8 February 2023 / Accepted: 10 April 2023 / Published online: 17 July 2023

Abstract
This paper begins with solving the linear elastodynamic equation with forcing by expanding it into Fourier series. We then proceed to prove the conservation laws of momentum, angular momentum, and energy. We intend the paper to provide a computational demonstration for modal analysis by showing that eigenmodes and frequencies of vibration of a free-suspending horse match with the modal analysis results of the horse after a short-impulse impact of the horse with a wall. The horse CAD model has to be modified to contain a rigid body portion to prevent the rotational-tumbling modes. A fast Fourier transform is applied to the sensorial time series data in the calculation of the vibration frequencies. One can see that many low-frequency modes and data match these modal analysis results.

Keywords Animal motions · Eigenfunction expansions · External forcing · Frequency matching · Sensors

Mathematics Subject Classification 92-08 · 92-10 · 92C10

1 Introduction

In Part I [1] of this series of papers, we have studiously computed and displayed the modes of motion of a horse and a camel. As can be seen, there are many types of movements by the various parts of those two animals. Some modes can be readily recognized to be natural and common and can be associated with the walking movements

---

G. Chen—on Development Leave from Texas A&M University.

✉ Goong Chen
gchen@math.tamu.edu

Extended author information available on the last page of the article

of horses and camels. But a few others appear to be less so. Therefore the question arises as to whether such modes are just computational curiosities or, rather, they are *genuine* fundamental modes of motion of the animals. The main purpose of this paper, Part II, is to demonstrate to the reader that, indeed, (nearly) all of the low-frequency modes of motion are *naturally occurring*, and can be *observed* in the real world of the lives of us or that of the animals. In a large sense, this paper is intended as a "validation" of sorts for its predecessor, Part I. Indeed, as far as theory is concerned, the present paper should constitute a grounding of Part I [1].

Nevertheless, when we used the CAD models of either a horse or a camel from Part I for our intended purpose, we have encountered unexpected technical difficulties. Our way of thinking is to create a (timewise) short pulse on the horse and then check the motion of the horse as a response. The corresponding motion of the horse, after the pulse of external forcing has terminated, should be close to a series expansion of eigenmodes of the horse. We will take *sensorial recordings* at several key positions, such as legs, ears, head and tail as time series. These time series are then subject to Fourier analysis by taking their fast Fourier transform. The transformed function(s) should display prominent peaks associated with the natural frequencies of vibration corresponding to the eigenmodes as displayed in Part I of our papers.

The reason for the technical difficulties we just mentioned is that the horse's body is approximately modeled as an elastic body. The short pulse we have in mind is the imparting of an impact force when that horse collides with a wall. The collision's impact force acts on the horse's body only briefly, during the rather short period of the horse's contact with the wall. As our model of the horse does not contain any bones and is purely elastic, after collision the horse would bounce off the wall just like a ball, tumbling end over end a few times. Such tumbling, to a large extent, consists of rotational and translational modes, plus vibrational modes. Such rotational and translational modes have been identified in Part I [1, Sect. 3, Theorem 3.1] as elements in the 6-dimensional null space of the elastodynamic operator with the force-free boundary condition. From the sensorial data, unfortunately for the time being, we are not able to filter out the rotational modes therein. We believe this technical difficulty is not insurmountable, but it would require a considerable amount of time to treat it. Not without some hesitation, eventually we have decided to take an "expedient" measure by inserting some solid rigid body inside the body of the horse, which serves as something like a bone structure and, then, it can prevent the occurrences of rotational tumbling of the horse body. This choice then makes the present study feasible.

The organization of the paper is as follows:

In Sect. 2, we describe the mathematical rudiments and the technical difficulties as mentioned in the above. In Sect. 3, we show the re-modeled horse and the pertinent data on its vibrational modes. In Sect. 4, we carry out the fast Fourier transform for the sensorial time series of a numerical experiment of a horse impacting a wall, and demonstrate the Fourier frequency decomposition property, all done through supercomputer simulations. A short summary is given in Sect. 5.

2 Solutions of a Distributed Parameter System with Forcing: A Preliminary Computer Simulation of a Horse Impacting on a Wall

2.1 Dynamics: An Example of a Horse Colliding with a Wall

The gist of this paper can be more easily understood through the viewing of a motion sequence as shown in Fig. 1 and the corresponding dynamical motion video. For this motion, an elastic model of the horse as in Part I [1] is used. There is no floor, but a rigid wall is erected on the left side of the spatial domain. The horse is moving leftward at speed 0.1 m/s and colliding with the wall. After a short duration of impact δt, the horse bounces and moves to the right. This bouncing of the horse has triggered a rotational mode and causes its body to tumble (approximately) one full cycle about the x-axis. The tumbling motion also contains vibrations of the horse body, which are especially noticeable in the legs, tail, ears and head. Visually, one can confirm that the vibration of the horse body contains features of the various modal shapes. This is the way it is supposed to be: the motion of vibration should be decomposable into a combination of time-harmonic eigenmodes.

In theory, it is possible to perform Fourier analysis on the motion as shown in Fig. 1. However, after some effort, so far we have not been able to produce effective algorithms and computer codes that can analyze the tumbling motion (namely, the rotational part of the) motion of the horse). The resolution of this difficulty will demand more time resources.

By analyzing these situations, we believe that the elastic, tumbling motion could very well be caused by the lack of any bone and skeletal structure in the horse. We somehow need to steady the motion of the horse so that tumbling will not occur. We tried, and found an *expedient measure/design* that can achieve this purpose by adding a solid, rigid block of mass within the horse body, as displayed in Fig. 2.

With the new horse CAD model, we now repeat the computing experiments in Fig. 1. What we have obtained is shown in Fig. 3.

Our main objective in this paper is to perform Fourier analysis on the motion in Fig. 3.

Before we move on to the next few sections, a few words are in order regarding *sensor measurements*. It is known from mechanical engineering and physics that various types of physical quantities can be measured by the designs of gauges and sensors, as follows:

acceleration: accelerometers [2]
velocity: velocimeters/speedometers [3]
displacement: laser displacement sensors [4]
force and pressure: transducers, strain gauges, load cells,... [5]

These are just some examples. When we perform signal or Fourier analysis of animal motion, in principle, we should be able to analyze any or all of the above physical variables. Nevertheless, in practice, the story is different: certain variable(s) will always be easier to measure or process than others. In our subsequent treatments, we will be choosing the *velocity variable* as the one for frequency and Fourier analysis.

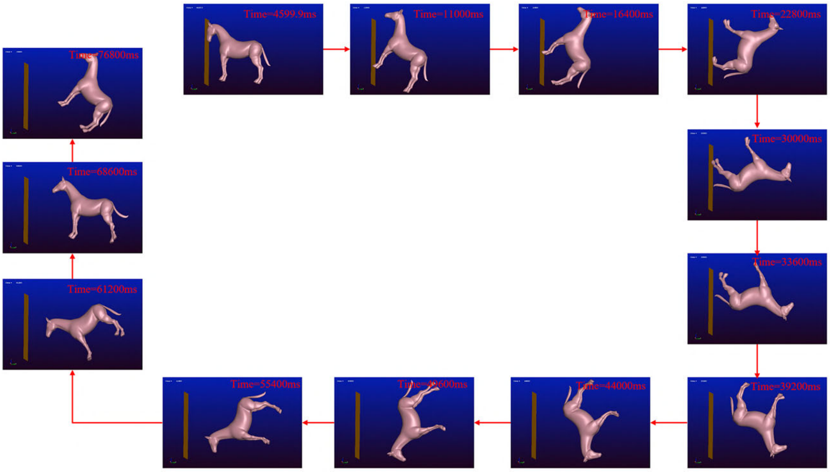

Fig. 1 A horse is moving with velocity 7 cm/s leftward. It collides with a rigid wall and then tumbles. Its body rotates 360 degrees around the x-axis. Here the motion sequence is represented by a series of snapshots. Please see video https://drive.google.com/file/d/1AkMo0U5X3VbDzOCa6oCIgCGqTpNEbfuR/view for the continuous dynamic motion

2.2 Solutions of the Elastodynamic Vibration Equation in Two Invariant Subspaces

We consider a vibration equation cast in the form of Eq. (4.1) in Part I [1]. First, we treat an abstract linear differential equation:

$$\begin{cases} \dfrac{\mathrm{d}}{\mathrm{d}t}\begin{bmatrix} \boldsymbol{u}_1(t) \\ \alpha\boldsymbol{u}_2(t) \end{bmatrix} = \begin{bmatrix} 0 & 1/\alpha \\ A & 0 \end{bmatrix}\begin{bmatrix} \boldsymbol{u}_1(t) \\ \alpha\boldsymbol{u}_2(t) \end{bmatrix} + \begin{bmatrix} 0 \\ \boldsymbol{f}(t) \end{bmatrix}, & 0 < t < \infty, \alpha > 0 \text{ is given}, \\ \begin{bmatrix} \boldsymbol{u}_2(t) \\ \alpha\boldsymbol{u}_2(t) \end{bmatrix}_{t=0} = \begin{bmatrix} \boldsymbol{u}_1(0) \\ \alpha\boldsymbol{u}_2(0) \end{bmatrix} \text{ is given}, \end{cases} \tag{2.1}$$

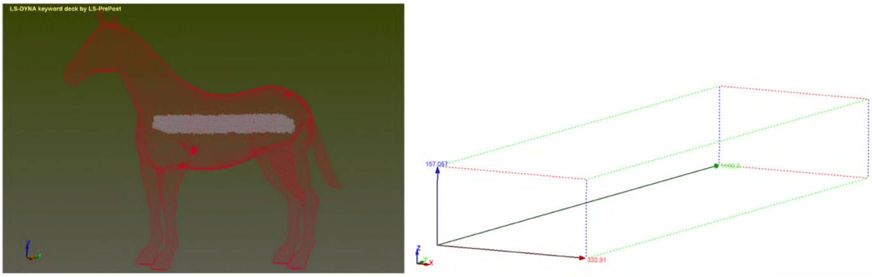

Fig. 2 **a** A block of solid, rigid mass is imbedded within the torso of the horse. This is intended as an offset mechanism for the lack of bone and skeletal structures in the horse (and, above all, it has the intended effect). The density of the block of mass is identical to that of the surrounding material of the horse body. **b** The exact description of the block is shown here. Coordinates of the origin are (– 0.17, – 0.56, 1.10) in the unit of m (meter). The dimensions of the rectangular block and the coordinates of some vertices are indicated. Every other system CAD parameter remains unchanged

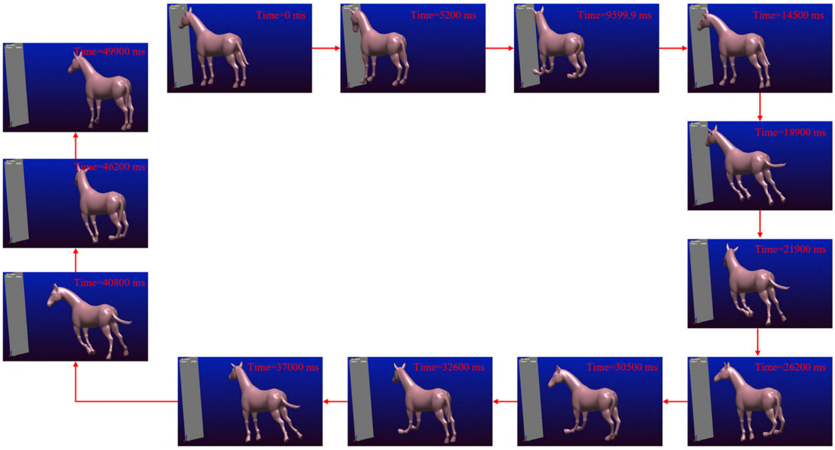

Fig. 3 This is a rerun of the simulation experiment similar to that of Fig. 1. A horse is moving with velocity 10 cm/s leftward, colliding with a rigid wall, but there is no tumbling. Rather, the horse is bounced backward to the right. The motion sequence is represented by a series of snapshots. Please see video https://drive.google.com/file/d/1Rj5nYZSnjZmG22ao3ikb0cu9Ca4o_kzE/view for the continuous dynamic motion

in a Hilbert space H, where A is an unbounded, densely defined, linear self-adjoint operator with domain $D(A)$, satisfying the compact resolvent property:

There exists a $\lambda_0 \in \mathbb{R}$ such that

$$R(\xi; A) \overset{\text{def.}}{=} (\xi I - A)^{-1} : H \to H \text{ is compact,} \tag{2.2}$$

for all $\xi > \lambda_0$.

Without loss of generality, we assume that $\lambda_0 = 0$. We further assume that $-A$ is a semi-positive operator:

$$\langle (-A)\boldsymbol{u}, \boldsymbol{u} \rangle_H \geq 0, \text{ for all } u \in D(A).$$

Then A has a complete orthogonal basis

$$\left\{\phi_{0,j} \mid j = 1, 2, \ldots, n_0\right\} \cup \{\phi_k \mid 1 \leq k < \infty\} \subseteq H, \text{ for some } n_0 \geq 1, \tag{2.3}$$

such that

$$\begin{aligned} A\phi_{0,j} &= 0, \quad j = 1, 2, \ldots, n_0; \\ A\phi_k &= -\mu_k^2 \phi_k, \quad 1 \leq k < \infty, 0 < \mu_1 \leq \mu_2 \leq \cdots \leq \mu_n \leq \cdots \to \infty; \\ \left\langle \phi_{0,j_0}, \phi_{0,k_0} \right\rangle_H &= \left\langle \phi_{0,j_0}, \phi_j \right\rangle_H = \left\langle \phi_j, \phi_k \right\rangle_H \\ &= 0, \text{ for any } j_0, k_0 : 1 \leq j_0, k_0 \leq n_0; \; j, k : 1 \leq j, k < \infty, \; j_0 \neq k_0, \; j \neq k. \end{aligned} \tag{2.4}$$

Corresponding to the partition (2.3), we have the orthogonal decomposition

$$H = H_0 \oplus H_1;\ H_0 = \operatorname{span}\left\{\phi_{0,j} \mid j = 1, 2, \ldots, n_0\right\},\ H_1 = \operatorname{span}\left\{\phi_k \mid 1 \le k < \infty\right\}. \tag{2.5}$$

The semi-positive operator $-A$ defines a positive semi-definite inner product $<,>_{\widetilde{H}}$ and an inner product space $\widetilde{H}$ by

$$\langle \boldsymbol{u}_1, \boldsymbol{u}_2 \rangle_{\widetilde{H}} = \left\langle (-A)^{1/2}\boldsymbol{u}_1, (-A)^{1/2}\boldsymbol{u}_2 \right\rangle_H, \tag{2.6}$$

for all $\boldsymbol{u}_1, \boldsymbol{u}_2 \in D(A^{1/2})$, where $A^{1/2}$ is the square root of the operator of A.

The orthogonal basis (2.3) induces an orthogonal decomposition

$$\widetilde{H} = H_0 \oplus \widetilde{H}_1, \quad \widetilde{H}_1 \overset{def.}{=} \widetilde{H} \cap H_1.$$

Note that $\widetilde{H}_1$ is now itself a Hilbert space with inner product (2.6).

Also note that $\{\phi_k | 1 \le k < \infty\}$, after a simple normalization, becomes an orthonormal basis for $\widetilde{H}_1$, i.e.,

$$\left\langle \phi_j, \phi_k \right\rangle_{H_1} = 0 \quad \text{if } j \ne k, \quad \|\phi_i\|_{H_1} = 1, \quad \text{for all } 1 \le j, k < \infty.$$

We now consider the solution of (2.1). It is given in terms of two invariant subspaces $H_0 \times H_0$ and $\widetilde{H}_1 \times H_1$.

Theorem 1 *(i) Let $\boldsymbol{f}(t) \equiv 0$ in the differential equation (2.1). If the initial condition satisfies*

$$\begin{bmatrix} \boldsymbol{u}_1(0) \\ \alpha \boldsymbol{u}_2(0) \end{bmatrix} \in H_0 \times H_0, \tag{2.7}$$

then the solution satisfies

$$\begin{bmatrix} \boldsymbol{u}_1(\cdot) \\ \alpha \boldsymbol{u}_2(\cdot) \end{bmatrix} \in C^\infty\left([0,\infty), H_0\right) \times C^\infty\left([0,\infty), H_0\right), \tag{2.8}$$

with the explicit representation

$$\begin{bmatrix} \boldsymbol{u}_1(t) \\ \alpha \boldsymbol{u}_2(t) \end{bmatrix} = \begin{bmatrix} \boldsymbol{u}_1(0) + t\boldsymbol{u}_2(0) \\ \alpha \boldsymbol{u}_2(0) \end{bmatrix}, \quad t \ge 0. \tag{2.9}$$

(ii) If $\boldsymbol{f}(\cdot)$ in (2.1) satisfies $\boldsymbol{f} \in L^2(0, \infty; H_0)$, then (2.1) has a mild solution satisfying

$$\begin{bmatrix} \boldsymbol{u}_1(t) \\ \alpha \boldsymbol{u}_2(t) \end{bmatrix} = \begin{bmatrix} \boldsymbol{u}_1(0) + t\boldsymbol{u}_2(0) + \frac{1}{\alpha}\int_0^t (t-s) f(s) ds \\ \alpha \boldsymbol{u}(0) + \int_0^t f(s) ds \end{bmatrix}, t \ge 0. \tag{2.10}$$

Proof One can directly verify that (2.9) is the (unique) solution to the homogeneous equation (2.1) when $\boldsymbol{f}(t) \equiv 0$. The mild solution (2.10) follows from the variation of parameters formula.

Theorem 2 *Consider Eq.* (2.1) *with given initial condition and forcing function satisfying, respectively,*

$$\begin{bmatrix} \boldsymbol{u}_1(0) \\ \alpha \boldsymbol{u}_2(0) \end{bmatrix} \overset{def.}{=} \begin{bmatrix} \boldsymbol{u}_1^0 \\ \alpha \boldsymbol{u}_2^0 \end{bmatrix} \in \widetilde{H}_1 \times H_1,\ \bar{\boldsymbol{f}}(\cdot) \in L^2\left(0, \infty; H_1\right).$$

Then (2.1) *has a unique solution represented in terms of eigenfunction expansions as*

$$\begin{bmatrix} \boldsymbol{u}_1(t) \\ \alpha \boldsymbol{u}_2(t) \end{bmatrix} = \sum_{n=1}^{\infty} \begin{bmatrix} \cos \omega_n t \left\langle \boldsymbol{u}_1^0, \phi_n \right\rangle_{\widetilde{H}} \phi_n + \frac{\alpha}{\omega_n} \sin \omega_n t \left\langle \boldsymbol{u}_2(0), \frac{\phi_n}{\sqrt{\alpha}\omega_n} \right\rangle_H \frac{\varphi_n}{\sqrt{\alpha \cdot \omega_n}} \\ -\omega_n \sin \omega_n t \left\langle \boldsymbol{u}_1^0, \phi_n \right\rangle_{\widetilde{H}} \phi_n + \alpha \cos \omega_n t \left\langle \boldsymbol{u}_2(0), \frac{\phi_n}{\sqrt{\alpha}\omega_n} \right\rangle_H \frac{\phi_n}{\sqrt{\alpha}\omega_n} \end{bmatrix}$$
$$+ \int_0^t \begin{bmatrix} \frac{1}{\omega_n} \sin \omega_n (t-\tau) \left\langle f(\tau), \frac{\phi_n}{\sqrt{\alpha}\omega_n} \right\rangle_H \frac{\phi_n}{\sqrt{\alpha}\omega_n} \\ \cos \omega_n (t-\tau) \left\langle f\left(\tau\right), \frac{\phi_n}{\sqrt{\alpha}\omega_n} \right\rangle_H \frac{\phi_n}{\sqrt{\alpha}\omega_n} \end{bmatrix} \mathrm{d}\tau$$

Proof The calculations essentially follow from the exponential matrix formula

$$e^{\begin{bmatrix} 0 & 1/\alpha \\ -\mu_n^2 & 0 \end{bmatrix} t} = \begin{bmatrix} \cos \omega_n t & \frac{1}{\omega_n} \sin \omega_n t \\ -\omega_n \sin \omega_n t & \cos \omega_n t \end{bmatrix},$$

where $-\mu_n^2$ are the eigenvalues of A in (2.4), and $\omega_n = \mu_n / \sqrt{\alpha}$. The rest can be verified from straightforward calculations.

Theorems 1 and 2 provide a concrete formula for the realization of the *variation of parameters formula* of evolution semigroups as described in [6].

We can now return to the elasticity model, Eq. (3.1) in Part 1 [1]. By comparing [1, (3.1)], we understand the correspondences:

$$\begin{aligned} \alpha &\longleftrightarrow \rho, \\ A &= (\lambda + \mu) \nabla \cdot (\nabla) + \nabla^2, && (2.11) \\ H &= \left[L^2(\Omega) \right]^3, && (2.12) \\ H_0 &= \operatorname{span} \left\{ \begin{bmatrix} 0 \\ -x_3 \\ x_2 \end{bmatrix}, \begin{bmatrix} x_3 \\ 0 \\ -x_1 \end{bmatrix}, \begin{bmatrix} -x_2 \\ x_1 \\ 0 \end{bmatrix}, \begin{bmatrix} 1 \\ 0 \\ 0 \end{bmatrix}, \begin{bmatrix} 0 \\ 1 \\ 0 \end{bmatrix}, \begin{bmatrix} 1 \\ 0 \\ 0 \end{bmatrix} \right\} \\ &= \operatorname{span} \left\{ \phi_{0,j} \mid j = 1, 2, 3, 4, 5, 6 \right\} \quad \text{(i.e., } n_0 = 6 \text{ in (2.3)}, && (2.13) \end{aligned}$$

and the inner product in H_1 is:

$$\langle \boldsymbol{u}, \boldsymbol{v} \rangle_{H_1} = \int_\Omega \left[\lambda (\nabla \cdot \boldsymbol{u})(\nabla \cdot \boldsymbol{v}) + \sum_{i,j=1}^{3} \mu \left(\frac{\partial u_i}{\partial x_j} + \frac{\partial u_j}{\partial x_i} \right) \left(\frac{\partial v_i}{\partial x_j} + \frac{\partial v_j}{\partial x_1} \right] \mathrm{d}x, \tag{2.14}$$

2.3 Conservation of Energy, Momentum and Angular Momentum

Consider the homogeneous elastodynamic equation

$$\begin{cases} \rho \frac{\partial^2 \boldsymbol{u}(\cdot,t)}{\partial t^2} = (\lambda+\mu)\nabla(\nabla\cdot\boldsymbol{u}(\cdot,t)) + \mu\nabla^2\boldsymbol{u}(\cdot,t) \quad \text{on } \Omega, t>0, \\ \begin{bmatrix} \boldsymbol{u}(\cdot,t) \\ \boldsymbol{u}_t(\cdot,t) \end{bmatrix}\Bigg|_{t=0} = \begin{bmatrix} \boldsymbol{u}_0 \\ \boldsymbol{u}_1 \end{bmatrix} \in \widetilde{H}\times D(A) \qquad \text{(cf. (2.11) for A)}, \\ \sum_{i=1}^3 \boldsymbol{\sigma}_{ij} n_i = 0 \quad \text{for } j=1,2,3, \quad \text{on} \quad \partial\Omega, \end{cases} \tag{2.15}$$

where Ω is a bounded domain in $\mathbb{R}^3$,

$$\boldsymbol{\sigma}_{ij} = \boldsymbol{\sigma}_{ij}(\boldsymbol{u}) = \lambda(\nabla\cdot\boldsymbol{u})\delta_{ij} + 2\mu\left(\frac{\partial u_i}{\partial x_j} + \frac{\partial u_j}{\partial x_i}\right), 1\le i,j\le 3 \;\Big) \tag{2.16}$$

is the usual stress tensor; and $\boldsymbol{n} = (n_1, n_2, n_3)$ is the unit outward pointing normal vector on $\partial\Omega$. It has the nice properties of conservation of momentum, angular momentum, and energy, to be established in the following.

Lemma 1 (Adjointness transposition) *Assume that $\boldsymbol{u}$ and $\boldsymbol{v}$ are sufficiently smooth vector-valued functions on Ω. Let A, H and H_1 be defined, respectively, as in* (2.11), (2.12) *and* (2.14). *Then we have*

$$\langle A\boldsymbol{u}, \boldsymbol{v}\rangle_H - \langle \boldsymbol{u}, A\boldsymbol{v}\rangle_H = \sum_{i,j=1}^3 \int_{\partial\Omega} \left[\boldsymbol{\sigma}_{ij}(\boldsymbol{u}) n_i v_j - \boldsymbol{\sigma}_{ij}(v) n_i u_j\right] \mathrm{d}\sigma.$$

Proof Using integration by parts twice, we can directly check that

$$\begin{aligned} \langle A\boldsymbol{u}, \boldsymbol{v}\rangle_H &= \sum_{i,j=1}^3 \int_{\partial\Omega} \boldsymbol{\sigma}_{ij}(\boldsymbol{u}) n_i v_j \mathrm{d}\sigma - \langle \boldsymbol{u}, \boldsymbol{v}\rangle_{H_1} \\ &= \sum_{i,j=1}^3 \int_{\partial\Omega} \left[\boldsymbol{\sigma}_{ij}(\boldsymbol{u}) n_i v_j - \boldsymbol{\sigma}_{ij}(\boldsymbol{v}) n_i u_j\right] \mathrm{d}\sigma + \langle \boldsymbol{u}, A\boldsymbol{v}\rangle. \end{aligned}$$

Theorem 3 (Conservation of energy) *Assume that $\boldsymbol{u}$ satisfies the homogeneous elastodynamic system* (2.15) *with sufficiently smooth initial condition (u_0, u_1). Then for the elastodynamic energy defined by*

$$E(t) = \frac{1}{2}\int_\Omega \left[\rho\left|\frac{\partial \boldsymbol{u}}{\partial t}\right|^2 + \lambda|\nabla\cdot\boldsymbol{u}|^2 + \sum_{i,j=1}^3 \left(\frac{\partial u_i}{\partial x_j} + \frac{\partial u_j}{\partial x_i}\right)^2\right] \mathrm{d}x, \quad t\ge 0,$$

we have

$$E(t) = E(0), \textit{for all } t \ge 0,$$

Proof We have

$$\begin{aligned}\frac{d}{\mathrm{d}t}E(t) &= \int_{\Omega}\Big[\rho\boldsymbol{u}_{tt}\cdot\boldsymbol{u}_t + \lambda(\nabla\cdot\boldsymbol{u})\,(\nabla\cdot\boldsymbol{u}_t)\\ &\quad + \sum_{i,j=1}^{3}\left(\frac{\partial u_i}{\partial x_j}+\frac{\partial u_j}{\partial x_i}\right)\left(\frac{\partial u_{i,t}}{\partial x_j}+\frac{\partial u_{j,t}}{\partial x_i}\right)\Big]\mathrm{d}x\\ &= \cdots \text{ (by the proof of Lemma 2.3)}\\ &= \int_{\Omega}(\rho\boldsymbol{u}_{tt}-A\boldsymbol{u})\,\boldsymbol{u}_t\mathrm{d}x + \sum_{i,j=1}^{3}\int_{\partial\Omega}\sigma_{ij}(\boldsymbol{u})n_i u_{j,t}\mathrm{d}\sigma\\ &= 0.\end{aligned}$$

Theorem 4 (Conservation of momentum) *Assume the same conditions as in Theorem 3. Then we have*

$$\frac{\mathrm{d}}{\mathrm{d}t}\int_{\Omega}\rho\boldsymbol{u}_t\mathrm{d}x = \mathbf{0}.$$

Proof We have

$$\begin{aligned}\frac{\mathrm{d}}{\mathrm{d}t}\int_{\Omega}\rho\boldsymbol{u}_t\mathrm{d}x &= \int_{\Omega}\rho\boldsymbol{u}_{tt}\mathrm{d}x\\ &= \int_{\Omega}A\boldsymbol{u}\mathrm{d}x = \mathbf{i}\int_{\Omega}(A\boldsymbol{u})\cdot\mathbf{i}\mathrm{d}x + \mathbf{j}\int_{\Omega}(A\boldsymbol{u})\cdot\mathbf{j}\mathrm{d}x\\ &\quad + \mathbf{k}\int_{\Omega}(A\boldsymbol{u})\cdot\mathbf{k}\mathrm{d}x\end{aligned} \tag{2.17}$$

where $\mathbf{i}, \mathbf{j}, \mathbf{k}$ are the standard unit vectors along the directions of, respectively, the x_1, x_2 and x_3 axes. We have, by Lemma 1:

(continuing from (2.17) $=$ $\{\mathbf{i}\langle\boldsymbol{u}, A(\mathbf{i})\rangle_H + \mathbf{j}\langle\boldsymbol{u}, A(\mathbf{j})\rangle_H + \mathbf{k}\langle\boldsymbol{u}, A(\mathbf{k})\rangle\}$ + boundary integral terms.

However

$$A(\mathbf{i}) = A(\mathbf{j}) = A(\mathbf{k}) = \mathbf{0},$$

and all the boundary term are zero because

$$\sum_{i=1}^{3}\sigma_{ij}(\boldsymbol{u})n_i = 0, \text{ for } j = 1, 2, 3,$$

and

$$\sigma_{ij}(\mathbf{i}) = \sigma_{ij}(\mathbf{j}) = \sigma_{ij}(\mathbf{k}) = 0 \text{ for all } 1 \le i, j \le 3.$$

Theorem 5 (Conservation of angular momentum) *Assume the same conditions as in Theorem 3. Then we have*

$$\frac{\mathrm{d}}{\mathrm{d}t}\int_\Omega \rho \boldsymbol{r} \times \boldsymbol{u}_t dx = \boldsymbol{0},\ \textit{where}\ \boldsymbol{r} = \begin{bmatrix} x_1 \\ x_2 \\ x_3 \end{bmatrix}. \tag{2.18}$$

Proof We note that, for any 3-vector $\boldsymbol{w} = (w_1, w_2, w_3)$, we have

$$\boldsymbol{r} \times \boldsymbol{w} = \mathbf{i}\left(-w_2x_3 + w_3x_2\right) + \mathbf{j}\left(w_1x_3 - w_3x_1\right) + \mathbf{k}\left(-w_1x_2 + w_2x_1\right). \tag{2.19}$$

Therefore

$$\begin{aligned} \frac{\mathrm{d}}{\mathrm{d}t}\int_\Omega \rho \boldsymbol{r} \times \boldsymbol{u}_t \mathrm{d}x &= \int_\Omega \rho \boldsymbol{r} \times \boldsymbol{u}_{tt} \mathrm{d}x \\ &= \int_\Omega \boldsymbol{r} \times (A\boldsymbol{u})\mathrm{d}x \\ &= \mathbf{i}\int_\Omega A\boldsymbol{u} \cdot \boldsymbol{v}^{(1)}\mathrm{d}x + \mathbf{j}\int_\Omega A\boldsymbol{u} \cdot v^{(2)}\mathrm{d}x \\ &\quad + \mathbf{k}\int_\Omega A\boldsymbol{u} \cdot v^{(3)}\mathrm{d}x,\ (2, 10J), \end{aligned} \tag{2.20}$$

where $\boldsymbol{v}^{(1)}$, $\boldsymbol{v}^{(2)}$ and $\boldsymbol{v}^{(3)}$, according to (2.19), are defined by

$$\boldsymbol{v}^{(1)} = \begin{bmatrix} 0 \\ -x_3 \\ x_2 \end{bmatrix},\ \boldsymbol{v}^{(2)} = \begin{bmatrix} x_3 \\ 0 \\ -x_1 \end{bmatrix},\ \text{and}\ \boldsymbol{v}^{(3)} = \begin{bmatrix} -x_2 \\ x_1 \\ 0 \end{bmatrix}.$$

(Continuing from (2.20), using similar arguments as in the proof of Theorem 4) $\cdots \Rightarrow$

$$\frac{\mathrm{d}}{\mathrm{d}t}\int_\Omega \rho \boldsymbol{r} \times \boldsymbol{u}_t = 0,$$

because

$$A\left(\boldsymbol{v}^{(l)}\right) = \boldsymbol{0},\quad \boldsymbol{\sigma}_{ij}\left(\boldsymbol{v}^{(l)}\right) = 0, \text{ for } l = 1, 2, 3,\ 1 \le i, j \le 3.$$

In Figs. 4 and 5, we exhibit a numerical verification of Theorems 4 and 5, where the reader can see that the velocity and angular velocity of the horse in Fig. 1 remain constant.

Remark 1 The conservation of energy property as given in Theorem 3 is well understood through the work of [7, 8], for example. However, the conservation laws of momentum and angular momentum as given in Theorem 4 and 5 do not seem to have been stated elsewhere, to the best of our knowledge. □

Remark 2 The conservation law of momentum remains valid for the modified horse model and motion as shown in Fig. 3 as well (just as it does for those in Fig. 1).

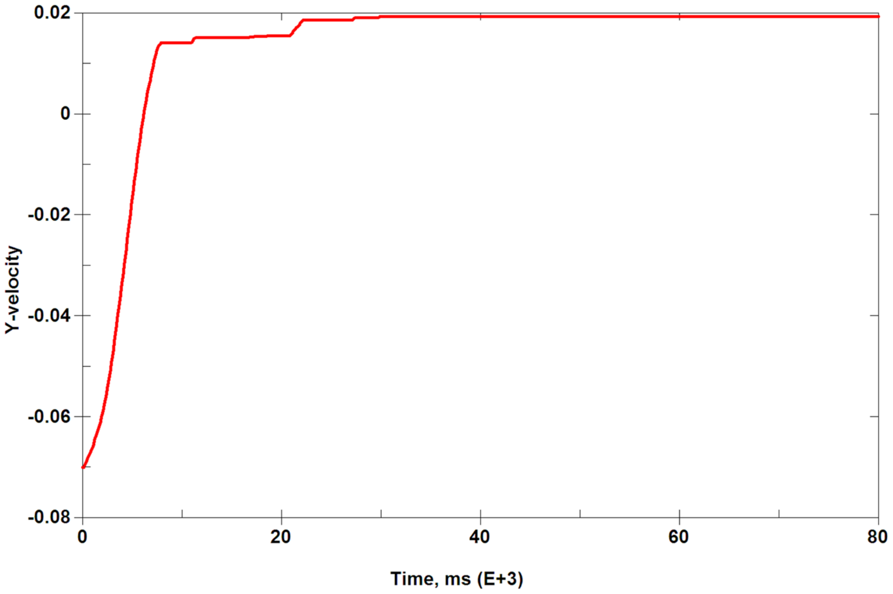

Fig. 4 Conservation of linear momentum (after the collision effects have ended) as demonstrated by the constant speed of the center of mass for the horse movement in Fig. 1

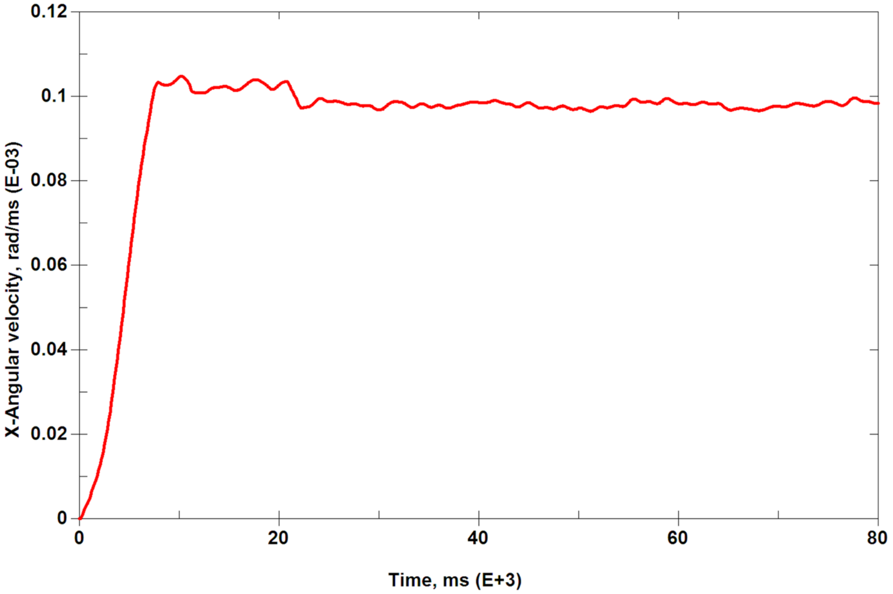

Fig. 5 Conservation of angular momentum (after the collision effects have ended) as demonstrated by the constant angular velocity (speed) of the center of mass for the horse movement in Fig. 1

Table 1 Choice of parameters for the constraints of the rigid material (inside the horse body as shown in Fig. 2) for Card 2 ([9, p. I-112])

Card 2	1	2	3	4–8
Variable	CMO	5	7	
Tyie	*F*	*F*	*F*	
Default	0	0	0	

The letter "*F*" means "default"

However, the conservation of angular momentum is no longer valid for the modified horse model in Fig. 3 because of restrictions imposed on rotation. □

3 Modal Analysis of the Horse with Constrained Motion

In this design of the horse, we are restricting the excitation of the rotating/tumbling motion and the z—(i.e., vertical) and y—(i.e., out of plane) axes motion of the horse so that the only degree of freedom of motion is horizontal, namely, along the x-axis. Implementation-wise, this is carried out using [9, I-112-114], where we use the following *card* for the *input specification* by LS-DYNA software as shown in Table 1:

Note that in Table 1 the values 5 and 7 are chosen to represent:

$5 \mapsto EQ.5$: constrained y and z displacements (for CON1);

$7 \rightarrow EQ.7$: constrained x, y and z rotations (for CON2).

Remark 3 LS-DYNA [10] is a commercial, non-open source software package. A user cannot see its inner workings. Thus we are unable to explain the technical details of the mathematics involved. This is a major disadvantage. However the most important thing here is that it works and the software subroutine has saved time in a major way. □

For the horse subjected to the given constraints, we again perform modal analysis. The first 100 time-harmonic modes, plus 6 rigid-body modes, are assembled and can be viewed in Fig. 6.

The first 100 eigenfrequencies are tabulated in Table 2.

4 Identification of Vibration Frequencies on Six Body Parts of the Horse

To measure the motion of the horse, we install six velocimeters on six points of the horse body: *left foreleg, left hindleg, nose/head, left ear, tail, and belly.* See Fig. 7. Note that for the *pointwise velocity sensorial* data to be available at arbitrarily given generally given points, an underlying assumption regarding the C^2 smoothness of the solution must be made. So let this be done. Thenceforth, each sensor can record the continuous 3D velocity motion time series at the given point. The Fourier transform of the motion data will then be taken. From the Fourier transform we hope to determine the frequencies in the time series and then compare them against the values of frequencies obtained and listed in Sect. 3.

Table 2 Frequencies of vibration: the first 100 modes with motion constraints

Mode 1–25 (kHz)		Mode 26–50 (kHz)		Mode 51–75 (kHz)		Mode 76–100 (kHz)		Mode 101–106 (kHz)	
1	2.715759E−07	26	2.930837E−04	51	7.703325E−04	76	1.125536E−03	101	1498337E−03
2	3.602931E−05	27	3.179854E−04	52	7.717913E−04	77	1.167815E−03	102	1.518146E−03
3	3.610336E−05	28	3205598E−04	53	7.818673E−04	78	1.182902E−03	103	1.531667E−03
4	3.959632E−05	29	3.337626E−04	54	7.829411E−04	79	1.186488E−03	104	1.538712E−03
5	3.969495E−05	30	3.788886E−04	55	7.833807E−04	80	1205581E−03	105	1.568952E−03
6	4.631360E−05	31	3.842441E−04	56	7.890813E−04	81	1.206319E−03	106	1.570220E−03
7	4.651378E−05	32	3.973247E−04	57	8235999E−04	82	1.214577E−03		
8	5.099507E−05	33	4.481104E−04	58	8.346187E−04	83	1234306E−03		
9	5.394512E−05	34	4.516666E−04	59	8.491141E−04	84	1237785E−03		
10	5433869E−05	35	4.647008E−04	60	8.904610E−04	85	1264662E−03		
11	7.522981E−05	36	4.661618E−04	61	9.044762E−04	86	1.291506E−03		
12	8.416913E−05	37	4.846366E−04	62	9205019E−04	87	1.293138E−03		
13	1.117575E−04	38	5.066996E−04	63	9.345583E−04	88	1296966E−03		
14	1.431492E−04	39	5.377253E−04	64	9.562835E−04	89	1.320541E−03		
15	1439073E−04	40	5.510445E−04	65	9.616839E−04	90	1.353852E−03		
16	1.792084E−04	41	5.617229E−04	66	9.911695E−04	91	1.358108E−03		
17	1.802689E−04	42	5.945405E−04	67	1.022874E−03	92	1.379990E−03		
18	1.957965E−04	43	6.073005E−04	68	1.041212E−03	93	1.394967E−03		
19	1.960237E−04	44	6.146262E−04	69	1.043273E−03	94	1.399757E−03		
20	2.042456E−04	45	6.583854E−04	70	1.064150E−03	95	1431968E−03		
21	2.313444E−04	46	6.680298E−04	71	1.096069E−03	96	1.434818E−03		
22	2.320187E−04	47	6.892461E−04	72	1.107420E−03	97	1435734E−03		
23	2.547546E−04	48	6.969647E−04	73	1.113228E−03	98	1.457717E−03		
24	2.561739E−04	49	7.064132E−04	74	1.116514E−03	99	1473158E−03		
25	2.854180E−04	50	7.545294E−04	75	1.120943E−03	100	1.478391E−03		

A total of 106 values are listed because the first few modes have zero frequencies and are trivial

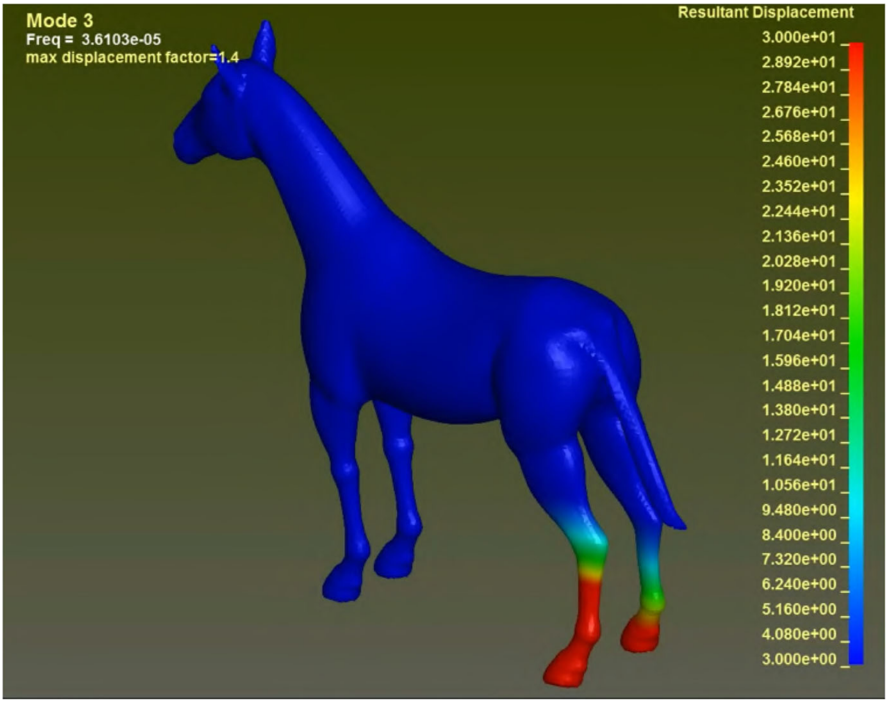

Fig. 6 (Viewable only online) Time-harmonic mode shapes of the first 100 modes of the horse with constraints of no rotation and no vertical and out-of-plane translations. Please note that there is now just one eigenvalue, namely, the horizontally translation, corresponding to the zero eigenfrequency, instead of the previous six degrees of freedom. Please click https://drive.google.com/file/d/1GcyVsSi3W_GIFA2ymyQJJaoMvfDE_UjD/view

In what follows, we divide the discussion into six subsections according to the respective body parts and sensor locations.

4.1 Frequency Analysis of Motion on the Left Foreleg

The motion time series is given in Fig. 8. Please note that there are three colored curves representing the data sets for each of the x, y and z components.

For each curve as given in Fig. 8, we take its fast Fourier transform using the software in [9, p. I-312]. The transformed curves are displayed in Fig. 9.

4.2 Frequency Analysis of Motion on the Left Fore leg

The motion time series is given in Fig. 11. As in the preceding section, there are three colored curves representing the data sets for each of the x, y and z directions.

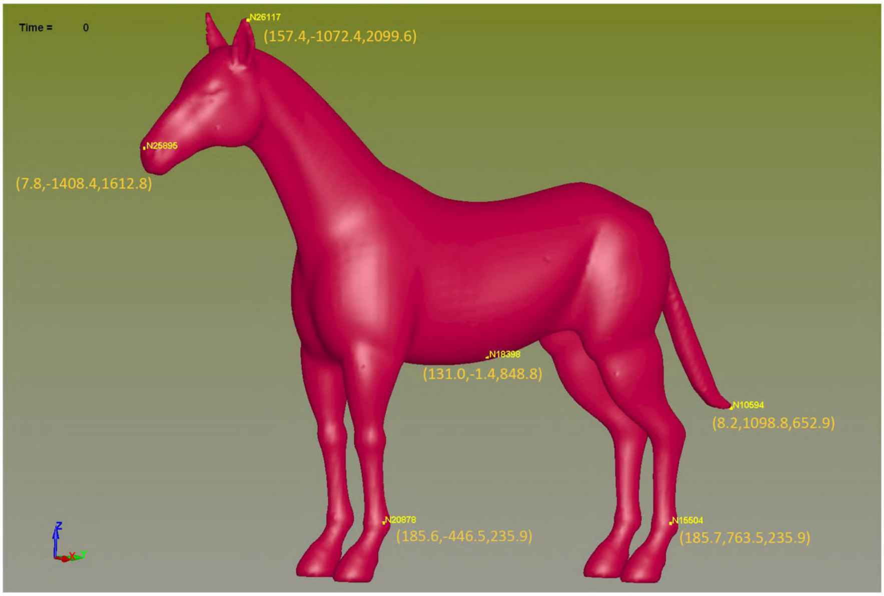

Fig. 7 Depiction of the six sensor locations on the horse body at left foreleg, left hindleg, nose/head, left ear, tail, and belly. The sensors' coordinates are also specified

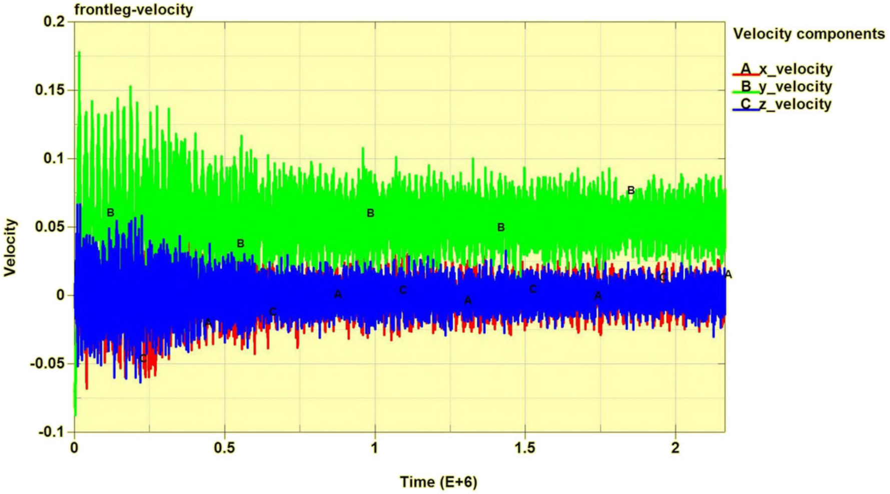

Fig. 8 There are three curves represented by three different colors for the three velocity components recorded on the left foreleg of the horse. In terms of magnitude, the green curve is the most prominent, representing the forward (and backward) horizontal velocity of the left foreleg (Color figure online)

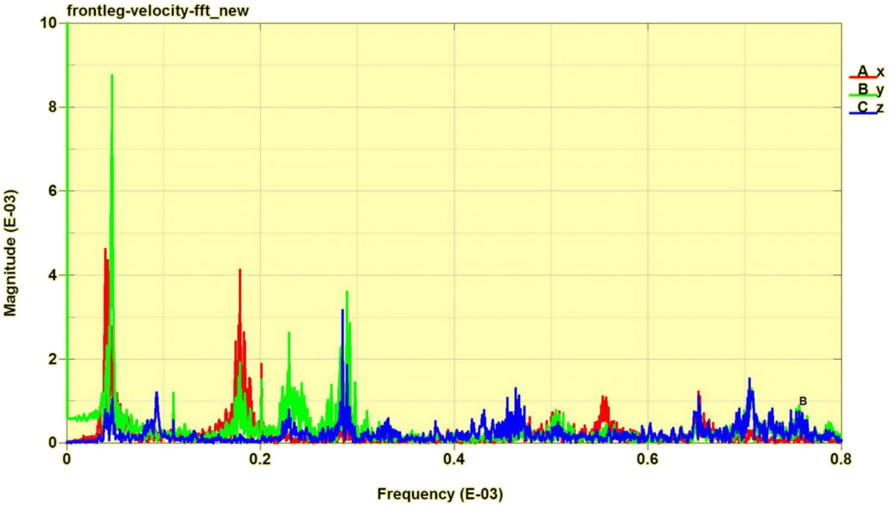

Fig. 9 The Fourier transforms of, respectively, the green, red and blue curves as displayed in Fig. 8. Please note that each peak is supposed to represent a frequency of vibration, especially the prominent ones (Color figure online)

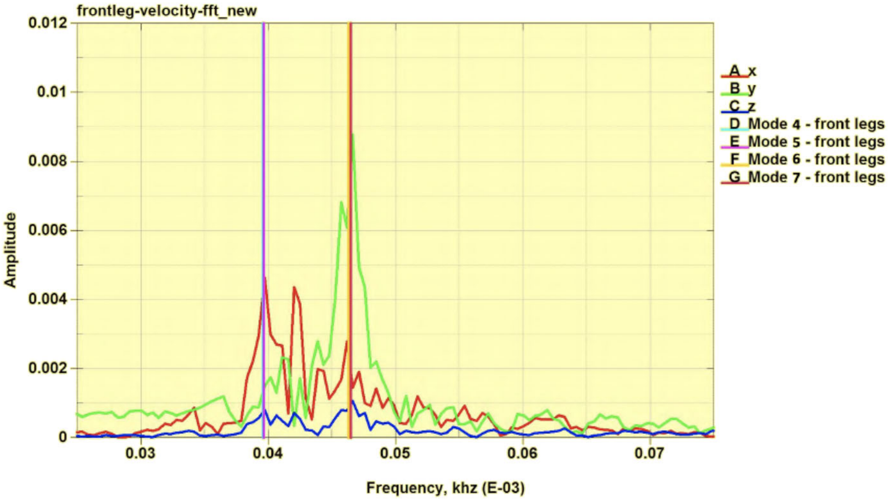

Fig. 10 Four different frequencies of vibration are marked, corresponding to Modes 4, 5, 6, and 7 of the eigen-modes concentrated on the left foreleg

4.3 Frequency Analysis of Motion on the Left Ear

The motion time series is given in Fig. 14. Please note that there are three colored curves representing the data sets for each of the x, y and z directions.

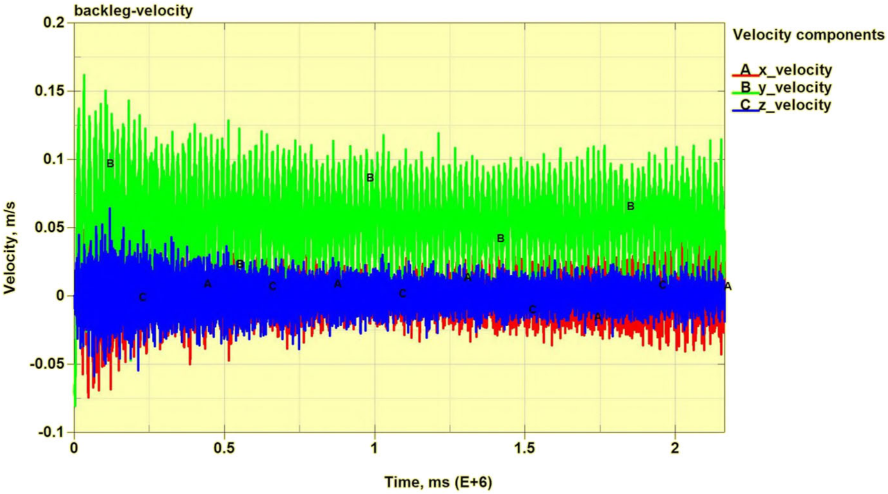

Fig. 11 There are three curves represented by three different colors for the three velocity components recorded on the left hindleg of the horse. In terms of magnitude, the green curve is the most prominent, representing the forward (and backward) horizontal velocity of the left hindleg (Color figure online)

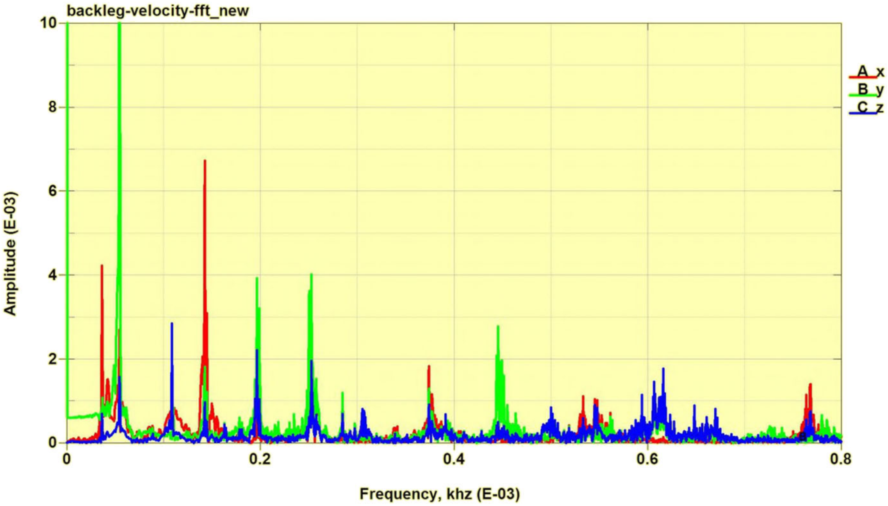

Fig. 12 The Fourier transforms of, respectively, the green, red and blue curves as displayed in Fig. 8. Please note that each peak is supposed to represent a frequency of vibration, especially the prominent ones (Color figure online)

4.4 Frequency Analysis of Motion on the Horse Nose

The motion time series is given in Fig. 17. As before, there are three colored curves representing the data sets for each of the x, y and z directions.

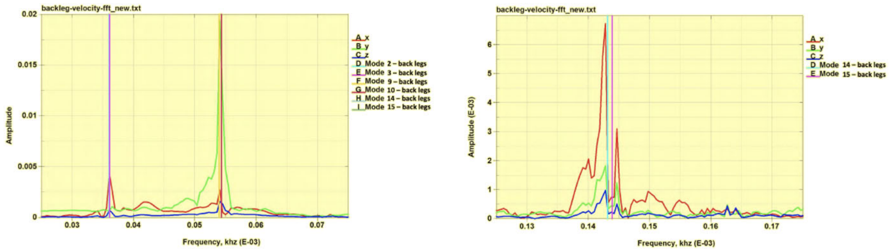

Fig. 13 Six different frequencies of vibration are marked, corresponding to Modes 2, 3, 9, 10, 14 and 15 of the eigenmodes concentrated on the left hindleg. Please note that the frequency plot is a zoomed-in view of the low-frequency portion of Fig. 12

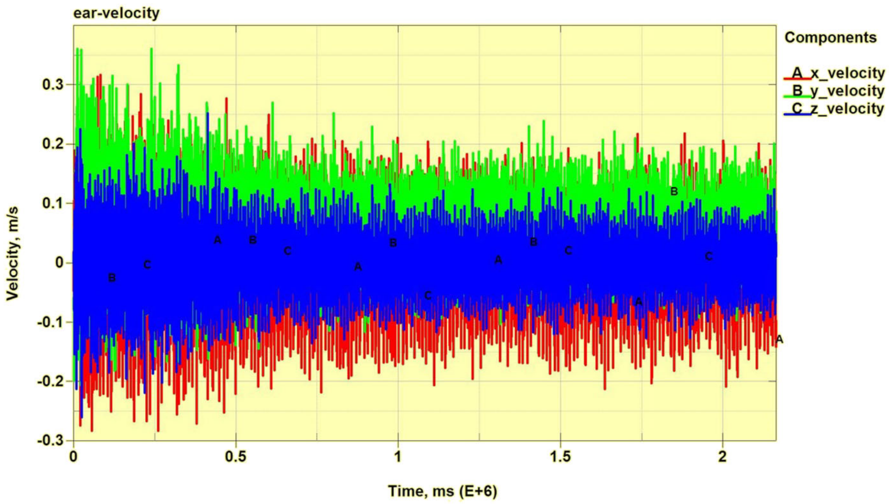

Fig. 14 There are three curves represented by three different colors for the three velocity components recorded on the left ear of the horse. In terms of magnitudes, the green and the red curves are the most prominent, representing, respectively, the lateral and vertical velocities of the left ear (Color figure online)

4.5 Frequency Analysis of Motion on the Horse Tail

The motion time series is given in Fig. 20. As before, there are three colored curves representing the data sets for each of the x, y and z directions.

4.6 Frequency Analysis of Motion on the Horse Belly

The motion time series is given in Fig. 23. As before, there are three colored curves representing the data sets for each of the x, y and z directions.

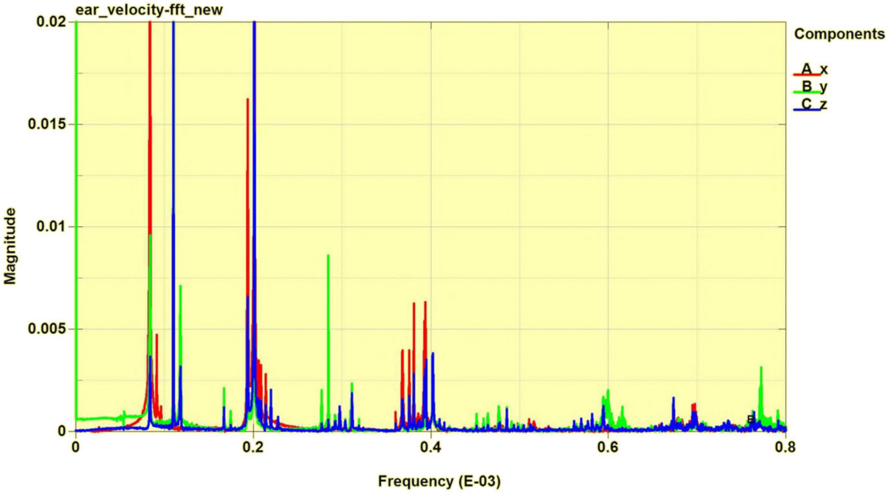

Fig. 15 The Fourier transforms of, respectively, the green, red and blue curves as displayed in Fig. 14. Please note that each peak is supposed to represent a frequency of vibration, especially the prominent ones (Color figure online)

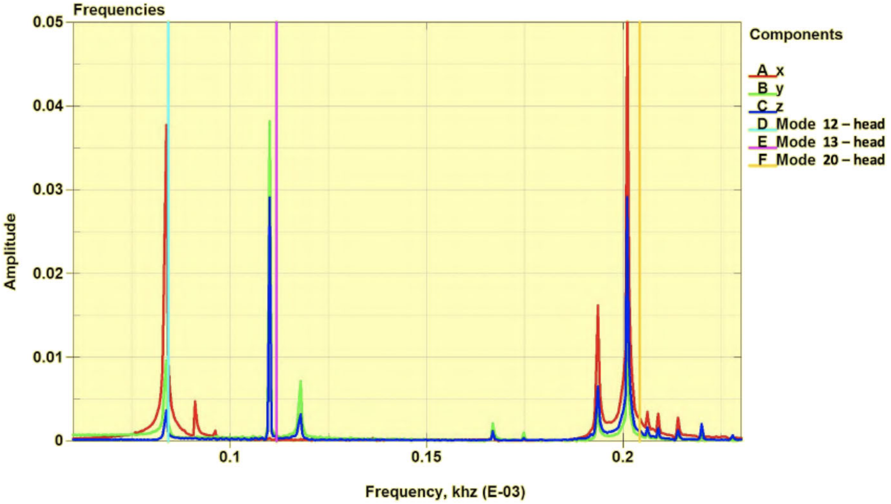

Fig. 16 Three different frequencies of vibration are marked, corresponding to Modes 12, 13 and 20 of the eigenmodes concentrated on the left ear. Please note that the frequency plot is a zoomed-in view of the low-frequency portion of Fig. 15

5 Concluding Remarks

The collection of our sensorial data (for a *naturally occurring motion of a horse* was executed through *an elastic collision of the horse with a wall*. Such a collisional motion was implemented via the LS-DYNA software but otherwise was not sufficiently well explained by us. Obviously, more mathematical understanding on this will be helpful.

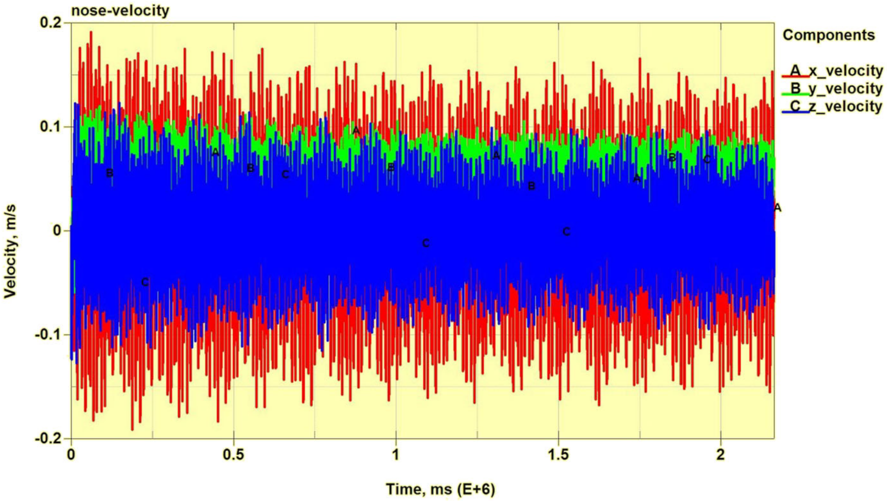

Fig. 17 There are three curves represented by three different colors for the three velocity components recorded on the left ear of the horse. In terms of magnitudes, the green and the red curves are the most prominent, representing, respectively, the lateral and vertical velocities of the left ear (Color figure online)

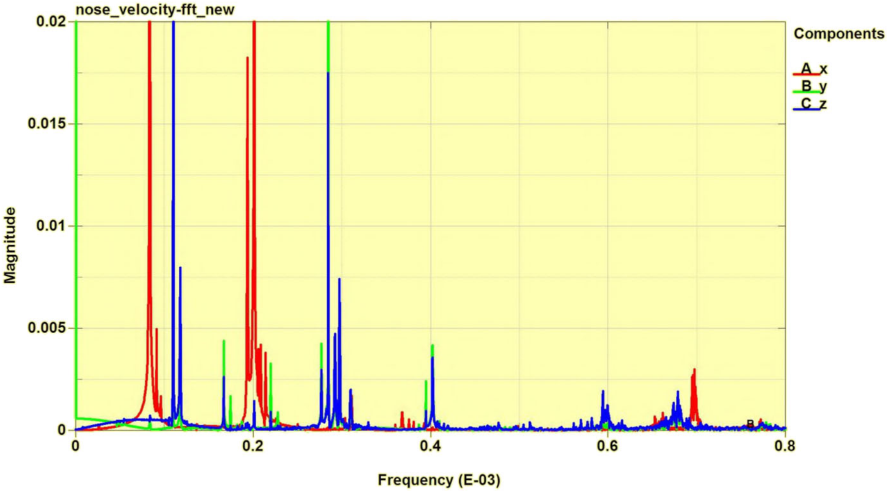

Fig. 18 The Fourier transforms of, respectively, the green, red and blue curves as displayed in Fig. 18. Each peak is supposed to represent a frequency of vibration, especially the prominent ones (Color figure online)

Here we wish to suggest a few references [11–13] for some further interest on this topic.

In this Part II, we believe we have significantly achieved the Fourier frequency decomposition of the fundamental modes of dynamic motion of a horse. The dynamics does not rely on specially selected initial conditions as that could well cause unspontaneous or manipulated dynamic motion of the horse. Rather, we let the horse collide with a wall, causing a short-duration impulse. Once the impulse ends, then there is no

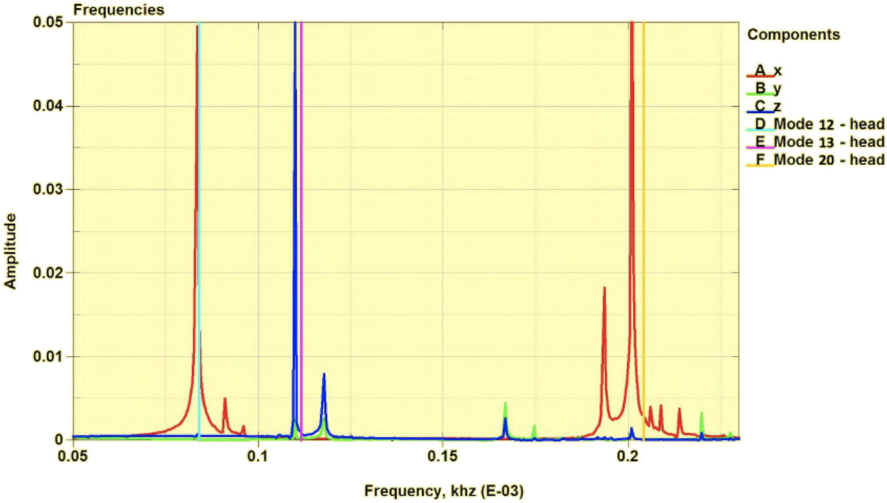

Fig. 19 Three different frequencies of vibration are marked, corresponding to Modes 12, 13 and 20 of the eigenmodes concentrated on the nose. Please note that the frequency plot is a zoomed-in view of the low-frequency portion of Fig. 18

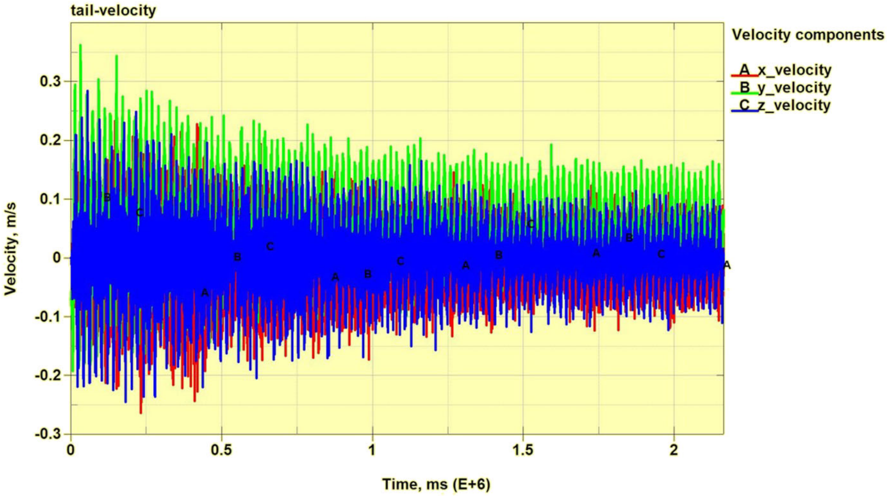

Fig. 20 There are three curves represented by three different colors for the three velocity components recorded on the left foreleg of the horse. In terms of magnitude, the red curve is the most prominent, which represents the up and down vertical velocity of the nose and head (Color figure online)

external forcing and the motion of the horse must be decomposable, through taking its fast Fourier transform, into a linear combinations of time-harmonic motion of the basic modes of vibration of the horse.

Nevertheless, our success with the Fourier decomposition is a qualified success as follows:

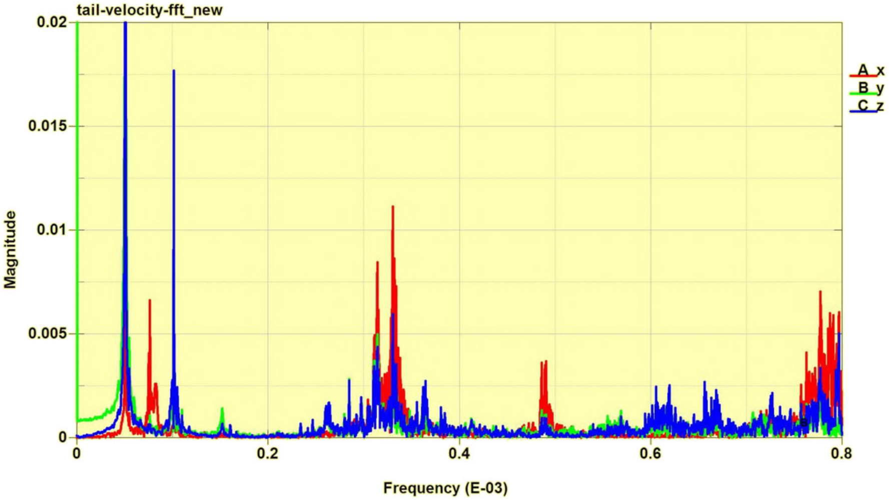

Fig. 21 The Fourier transforms of, respectively, the green, red and blue curves as displayed in Fig. 20. Each peak is supposed ta represent a frequency of vibration, especially the prominent ones (Color figure online)

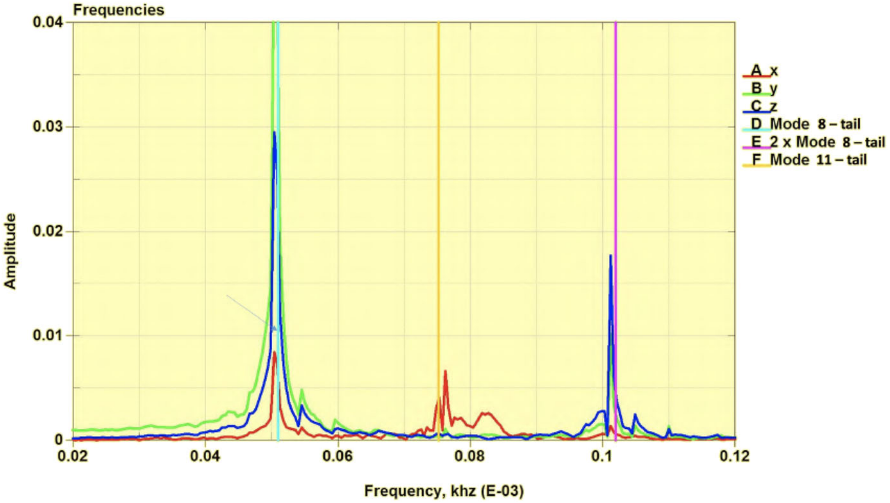

Fig. 22 Two different frequencies of vibration are marked, corresponding to Modes 8 and 11. the eigenmodes concentrated on the tail. Please note that the frequency plot is a zoomed-in view of the low-frequency portion of Fig. 21. Furthermore, we are able to identify a second harmonic generation, whose frequency is twice that of Mode 8

(i) We are, so far, unable to process the Fourier analysis of the tumbling/rotating effects of the horse body.

(ii) As a consequence of (i), we had to insert a rigid body inside the horse to have a desirable motion-constraint effect that eliminates the tumbling. This is, at least, somewhat unnatural.

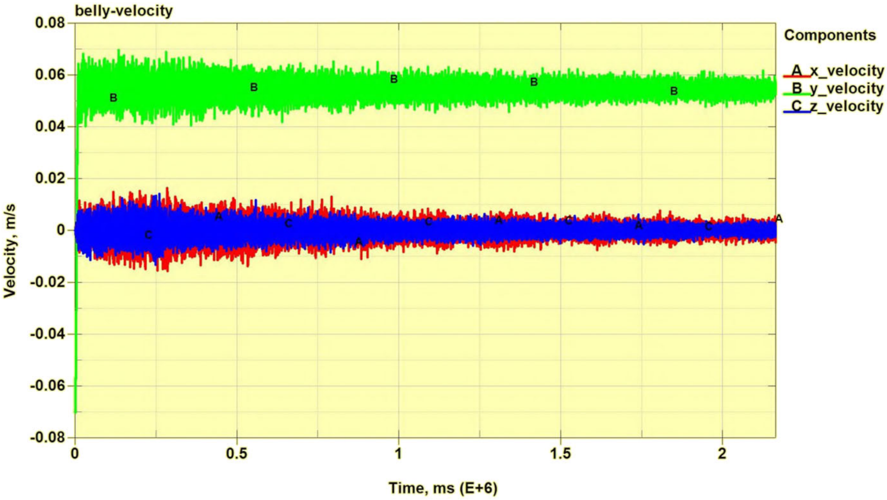

Fig. 23 Four different frequencies of vibration are marked, corresponding to Modes 4, 5, 6, and 7 of the eigen-modes concentrated on the left foreleg

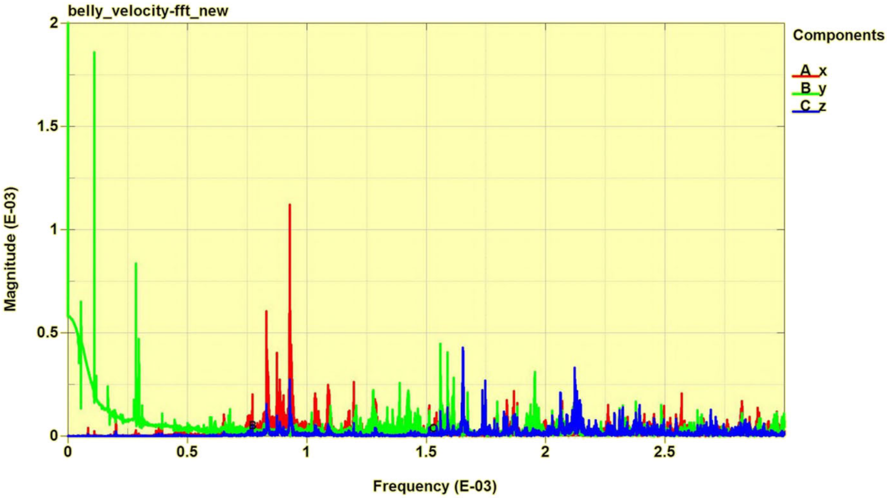

Fig. 24 The Fourier transforms of, respectively, the green, red and blue curves as displayed in Fig. 20. Each peak is supposed to represent a frequency of vibration, especially the prominent ones. An apparent inflection point here also appears to represent a frequency of vibration (Color figure online)

(iii) Some peaks on the Fourier-transformed spectrum cannot yet be identified with any eigenmodes. Some of those unidentified frequencies, we suspect, could be somehow related to the "aliasing" effect in digital signal processing.
(iv) More work needs to be done for some higher frequency modes.

Naturally, these are shortcomings that can be interesting topics for future research.

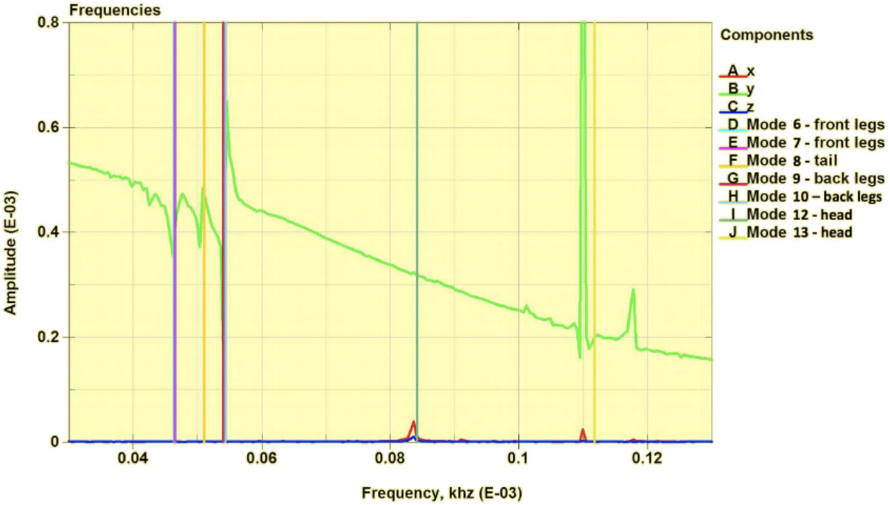

Fig. 25 Seven different frequencies of vibration are marked, corresponding to Modes 6. 7, 8, 9, 10, 12 and 13. These frequencies belong to eigenmodes concentrated on the left fore- and hind-legs, tail, and nose. Please note that the frequency plot is a zoomed-in view of the low-frequency portion of Fig. 24. Therefore this mixture of modes all bears some influence on the motion of the belly, as recorded at the belly sensor point

Acknowledgements We thank Prof. Jan Sokolowski for helpful suggestions. Tiexin Guo is supported by the National Natural Science Foundation of China (No.11671278 and No.11971483) and the Science and Technology Research Project of Chongqing Municipal Education Commission(KJ1706154). Pengfei Yao is supported in part by the National Science Foundation of China, grant No. 12071463, and by the special fund for Science and Technology Innovation Teams of Shanxi Province, Grants # 202204051002015. Junmin Wang is supported in part by the National Natural Science Foundation of China No. 62073037 and 12131008. Chunqiu Wei is supported by the Research Ability Improvement Program for Young Teachers of BUCEA (Grant No. X21031).

References

1. Chen, G., Huang, J., Wei, C.-Q., Yang, J., Scully, M.M., Sergeev, A., Chen, M.-C., Krantz, S.G., Yao, P.-F., Guo, T., Wang, J.-M.: Animal shapes, modal analysis, and visualization of motion (I): horse and camel. J Geom Anal. (2023). https://doi.org/10.1007/s12220-023-01339-1
2. Accelerometers: https://en.wikipedia.org/wiki/Accelerometer
3. Velocimeters/speedometers: https://en.wikipedia.org/wiki/Speedometer
4. Position sensors: https://en.wikipedia.org/wiki/Position_sensor
5. Piezoelectric sensors: https://en.wikipedia.org/wiki/Piezoelectric_sensor
6. Pazy, A.: Semigroups of Linear Operators and Applications to Partial Differential Equations, vol. 44. Springer, Berlin (1983)
7. Philippe, G.C.: Mathematical Elasticity, vol. I: Three-Dimensional Elasticity. North-Holland, Amsterdam (1988)
8. Lagnese, J.: Boundary stabilization of linear elastodynamic systems. SIAM J. Control Optim. **21**(6), 968–984 (1983)
9. LSTC: LS-DYNA Keyword User's Manual, Volume II—Material Models (Version 971 R6.1.0). https://ftp.lstc.com/anonymous/outgoing/jday/manuals/LS-DYNA_manual_Vol_II_R6.1.0.pdf
10. LSTC: Ansys LS-DYNA Multiphysics solver. https://www.ansys.com/products/structures/ansys-ls-dyna/

11. Lebeau, G., Schatzman, M.: A wave problem in a half-space with a unilateral constraint at the boundary. J. Differ. Equ. **53**(3), 309–361 (1984)
12. Nowak, M., Sokołowski, J., Żochowski, A.: Biomimetic approach to compliance optimization and multiple load cases. J. Optim. Theory Appl. **184**, 210–225 (2020)
13. Nowak, M., Sokołowski, J., Żochowski, A.: Justification of a certain algorithm for shape optimization in 3d elasticity. Struct. Multidiscip. Optim. **57**, 721–734 (2018)

Authors and Affiliations

Goong Chen[1,2,3] · Chunqiu Wei[4] · Alexey Sergeev[1] · Jing Yang[5] · Jingtong Kaya Huang[1] · Matthew M. Scully[1] · Ming-Chieh Chen[6] · Steven G. Krantz[7] · Pengfei Yao[8,9] · Tiexin Guo[10] · Junmin Wang[5]

[1] Department of Mathematics, Texas A&M University, College Station, TX 77843, USA

[2] Institute for Quantum Science and Engineering, Texas A&M University, College Station, TX 77843, USA

[3] Hsinchu Branch, National Center for Theoretical Sciences, National Tsing Hua University, Hsinchu, Taiwan, ROC

[4] Department of Mathematics and Data Science, Beijing University of Civil Engineering and Architecture, Beijing 100044, China

[5] School of Mathematics, Beijing Institute of Technology, Beijing 100081, China

[6] Department of Mechanical Engineering, Cheng Shiu University, Kaohsiung 83347, Taiwan, ROC

[7] Department of Mathematics, Washington University at St. Louis, St. Louis, MO 63130, USA

[8] Key Laboratory of Complex Systems and Data Science of Ministry of Education, School of Mathematics, Shanxi University, Taiyuan 030006, Shanxi, China

[9] Institute of Systems Science, Academy of Mathematics and Systems Science, Academia Sinica, Beijing 100190, China

[10] School of Mathematics and Statistics, Central South University, Changsha 410075, Hunan, China